JOURNAL OF GEOPHYSICAL RESEARCH, VOL. 113, C02024, doi:10.1029/2007JC004230, 2008

Application of a nested-grid ocean circulation model to Lunenburg Bay of Nova Scotia: Verification against observations

Li Zhai,[1] Jinyu Sheng,[1] and Richard J. Greatbatch[1]

Received 19 March 2007; revised 3 August 2007; accepted 21 November 2007; published 29 February 2008.

[1] A nested-grid ocean circulation modeling system is used to study the response of Lunenburg Bay in Nova Scotia, Canada, to local wind-forcing, tides, remotely generated waves, and buoyancy forcing in the summer and fall of 2003. Quantitative comparisons between observations and model results demonstrate that the modeling system reproduces reasonably well the observed sea level, temperature, salinity, and currents in the bay. Numerical results reveal that the spatial and temporal variability of temperature and salinity in the bay during the study period is mainly forced by the local wind stress and surface heat/freshwater fluxes, with some contribution from tidal circulation. In particular, the local heat balance on the monthly timescale is dominated by cooling due to vertical advection and warming due to horizontal advection and net surface heat flux, while high-frequency variations (timescales of 1–30 days) are mainly associated with vertical advection, i.e., wind-induced upwelling and downwelling. There is also a strong baroclinic throughflow over the deep water region outside Lunenburg Bay that is strongly influenced by wind-forcing. The vertically integrated momentum balance analysis indicates a modified geostrophic balance on the monthly timescale and longer, and is dominated by the pressure term and wind minus bottom stress in the high-frequency band.

Citation: Zhai, L., J. Sheng, and R. J. Greatbatch (2008), Application of a nested-grid ocean circulation model to Lunenburg Bay of Nova Scotia: Verification against observations, *J. Geophys. Res.*, *113*, C02024, doi:10.1029/2007JC004230.

1. Introduction

[2] Lunenburg Bay (hereafter LB) in Nova Scotia, Canada, is a shallow coastal embayment located on the southern coast of Nova Scotia, with a surface area of about 8 km by 4 km and a maximum water depth of 25 m (Figure 1). LB is shallow in the sense that its mean water depth ($\sim$15 m) is comparable to the typical turbulent Ekman layer thickness $0.1u_*f^{-1}$ of about 10 m in the region, where $f = 10^{-4}$, $u_* = (\tau/\rho)^{1/2}$ is friction velocity, and τ is the typical magnitude of the wind stress of $\sim$0.1 Pa. The dimension of LB is comparable to the first baroclinic Rossby radius of about 2 km of the bay, indicating that the Coriolis effect is important in the baroclinic dynamics in the bay [*Zhai et al.*, 2007]. In 2002, a multidisciplinary coastal observatory was established in LB (http://www.cmep.ca/bay; *Wang et al.*, 2007). The observatory has two major components: a real-time observational component and a coupled modeling component. Here we describe the physical part of the modeling system, and compare the model results against the observations to quantify the model performance. We also use the ocean circulation model to gain insight into the essential dynamics governing the baroclinic currents and thermal structure in the bay, and exchange of heat and salt between the bay and inner Scotian Shelf.

[3] The barotropic circulation in LB was studied in the past. *Sturley and Bowen* [1996] used a Galerkin spectral model to study the barotropic tidal jet and tidal asymmetry in LB, and *Thompson et al.* [1998] used the same model to interpret synthetic aperture radar images of the surface circulation in LB. More recently, *Sheng and Wang* [2004] used a z-level coastal circulation model (CANDIE) to study barotropic tides and nonlinear tidal dynamics in LB, and *Wang et al.* [2007] used the same model to simulate the storm-induced circulation in LB during Hurricane Juan in 2003. None of these previous efforts attempted to simulate the temperature and salinity structure and associated variability in the bay. *Zhai et al.* [2007] have shown that the observed temperature and salinity in LB had significant spatial and temporal variability in the summer and fall of 2003, and demonstrated the importance of both local (i.e., surface heating) and non-local (i.e., advective) processes based on the analysis of heat budget. The observed non-tidal currents were also found to have significant temporal variations, with the first EOF (empirical orthogonal function) mode correlated with the local wind-forcing, and the second EOF mode related to the vertical shear of the horizontal currents estimated from horizontal density gradients based on the thermal wind relation [*Zhai et al.*, 2007]. To further understand the dynamics of LB, the modeling system described here includes temperature and salinity as

[1]Department of Oceanography, Dalhousie University, Halifax, NS, Canada.

0148-0227/08/2007JC004230$09.00

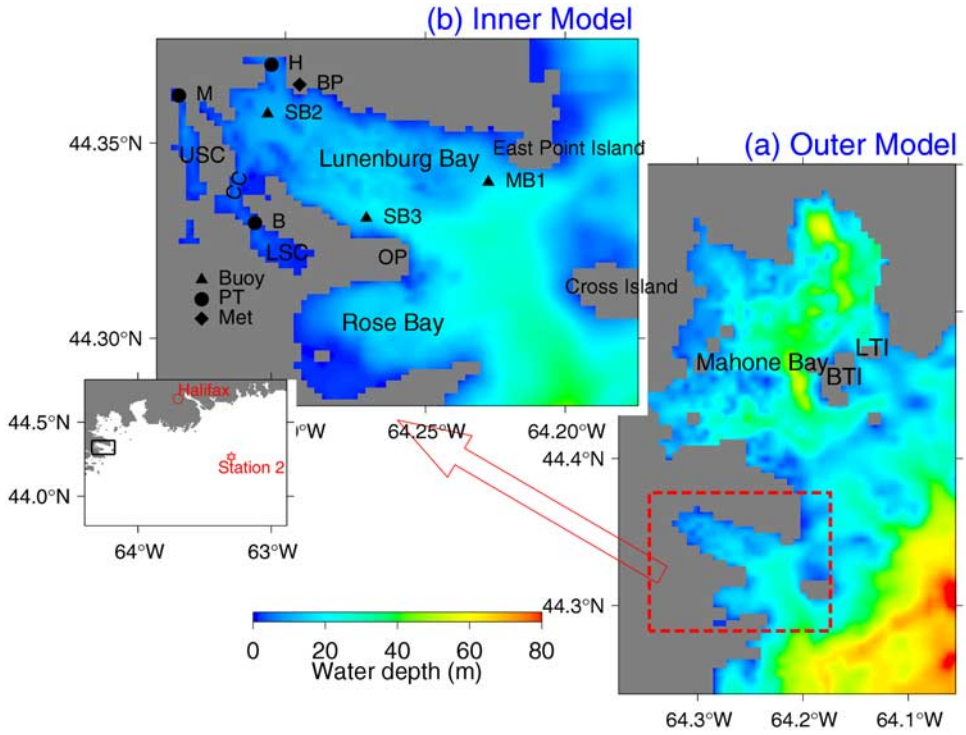

Figure 1. Major bathymetric features within the domains of (a) the outer model and (b) the inner model of the nested-grid modeling system. Abbreviations are used for Big Tancook Island (BTI), Cross Island (CI), Upper South Cove (USC), Lower South Cove (LSC), Corkum's Channel (CC), and Ovens Point (OP). The solid triangles denote the buoy locations. The solid circles denote the locations of pressure-temperature (PT) sensors. The solid diamond denotes the meteorological station. Inset shows a large area that covers inner Scotian Shelf, and Station 2 is marked by a star.

prognostic variables. Furthermore, the model for LB is nested inside a larger domain model including Mahone Bay, located to the northwest and "upstream" of LB in the sense of Kelvin wave propagation, creating a baroclinic version of the nested-grid coastal circulation modeling system introduced by *Sheng et al.* [2008].

[4] The arrangement of this paper is as follows. Section 2 outlines the nested-grid modeling system. Section 3 presents the simulated circulation and temperature fields during upwelling and downwelling events, and describes three additional numerical experiments designed to illustrate the dynamics. Section 4 assesses model performance based on the comparison of observations and model results. Section 5 examines the heat budget and section 6 examines the vertically integrated momentum balance. A summary and conclusions are given in section 7.

2. The Nested-Grid Circulation Modeling System

2.1. Ocean Circulation Model and Setup

[5] The nested-grid modeling system is based on the free surface version of CANDIE [*Lu et al.*, 2001; *Sheng and Wang*, 2004], which is a primitive equation model formulated in the finite difference form with a z-level in the vertical. The nested-grid system used in this paper has a fine-resolution inner model embedded in a coarse-resolution outer model (Figure 1). The outer model covers Mahone Bay (MB), Lunenburg Bay (LB) and Rose Bay (RB), with a horizontal resolution of ~500 m. The inner model covers LB and RB, with a horizontal resolution of ~200 m. The use of 200 m grid spacing ensures that the first three baroclinic radii of deformation in the bay (3.1 km, 1.4 km, and 0.9 km, respectively; see *Zhai et al.*, 2007) are reasonably resolved in the finer-resolution inner model. Both the inner and outer models have 24 z-levels with a vertical resolution of 1 m, except for 3 m for the top z-level, and 4.5 m below 20 m depth. It should be noted that the outer model does not resolve Upper South Cove (USC) and Lower South Cove (LSC). In comparison, the inner model does resolve the two coves, but resolves the mouth of USC poorly. As we will demonstrate later, although the inner model does not resolve the detailed circulation in the mouth and adjacent areas, it reproduces reasonably well the volume transport of the currents through the mouth.

[6] The nested-grid modeling system uses the hydrostatic and Boussinesq approximations in the model governing equations, and the 4th order numerics [*Dietrich*, 1997] and a flux limiter [*Thuburn*, 1996] to reduce numerical dispersion of the advection terms in the model. The modified version of the KPP (K-profile parameterization, *Large et al.*, 1994) vertical mixing scheme is used [*Durski et al.*, 2004], together with the horizontal mixing scheme of *Smagorinsky* [1963] for which the Prandtl number (the ratio between eddy diffusivity and viscosity) is set to 0.1. A quadratic bottom stress parameterization is used with a drag coefficient of 3×10^{-3}, except in the neighborhood of USC and LSC where a spatially variable and relatively larger

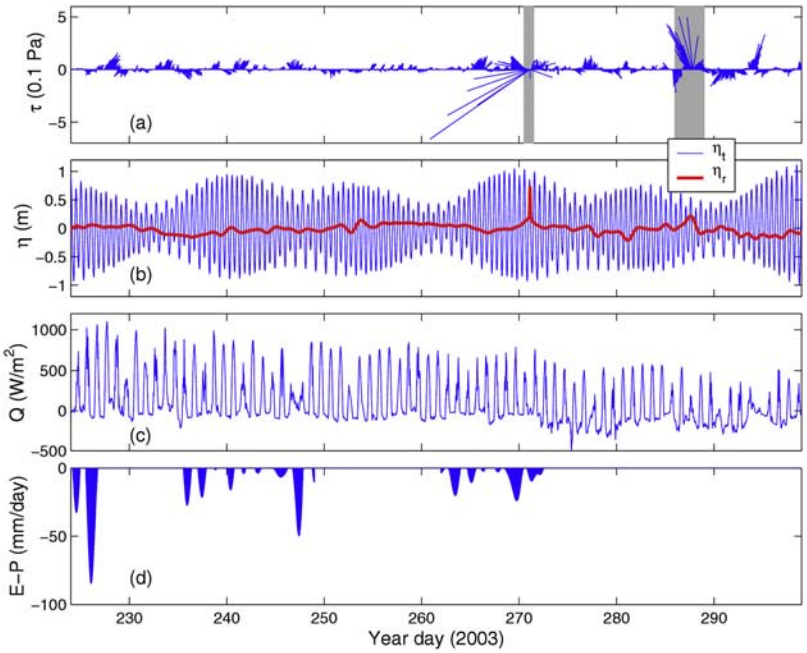

Figure 2. Time series of (a) wind stress at SB3, (b) tidal elevations η_t and remotely generated waves η_r, (c) net sea surface heat flux, and (d) diagnosed sea surface freshwater flux (*E-P*) from days 224 (13 August) to 299 (27 October) in 2003. The grey shaded vertical bars in (a) indicate the strong wind events discussed in the text. The sampling interval is 30 minutes.

drag coefficient is used [see *Sheng and Wang*, 2004, for details].

[7] The nested-grid modeling system is initialized from a state of rest with horizontally uniform, but vertically stratified temperature and salinity, and integrated for 75 days from 13 August (day 224) to 27 October (day 299), 2003. The initial vertical profiles of temperature and salinity in the top 25 m are based on the observations in LB, and below 25 m are based on the hydrographic surveys at station 2 on the inner Scotian Shelf (Figure 1) in the summer of 2003.

2.2. Model Forcings at Surface

[8] The external forcing to drive the nested-grid modeling system includes the wind stress and net sea surface heat flux constructed from the observations (Figure 2). A reader is referred to *Zhai et al.* [2007] for more information on the observations in the bay. The observed wind velocities at sites SB2 and SB3 in LB were highly similar, indicating that the wind velocity was nearly spatially uniform during the study period. For simplicity, the wind-forcing used to drive the modeling system is assumed to be spatially uniform and equal to that at SB3. It should be noted that the small-scale circulation in LB can be affected by the horizontal variation of the wind-forcing in the bay, as discussed by *Wang et al.* [2007]. There were two major wind events from days 224 to 229, 2003 (Figure 2a). The wind stress on day 271 (up to 1.4 Pa, 29 September) veered cyclonically as Hurricane Juan passed to the east of the study region, and on day 287 (27 October) the wind stress (up to 0.6 Pa) rotated anticyclonically in association with a low pressure system moving southward through southern Quebec to the west of the study region.

[9] The estimated net surface heat flux (Figure 2c) has significant daily and day-to-day variations. The monthly means indicate that the coastal water in LB gained heat in August (~200 W/m^2) and September (~150 W/m^2) but started losing heat in October of 2003 (~−10 W/m^2). The total surface heat flux seen by the model is given by

$$Q_{net} = Q^{input} + \beta(SST^o - SST^m), \tag{1}$$

where Q^{input} is the net surface heat flux taken from *Zhai et al.* [2007] (Figure 2c), SST^o is the observed sea surface temperature at MB1, SST^m is the model sea surface temperature, and β is the coupling coefficient defined as $\Delta z_1 \rho_0 c_p/\tau$, where Δz_1 is the thickness of the top z-level, c_p is the specific heat, τ is the restoring timescale set to 10 days. The part of the net surface heat flux associated with downward solar irradiance is distributed as a function of depth and represented by the expression suggested by *Paulson and Simpson* [1977] and given by

$$I = Q_I\left[Re^{z/\xi_1} + (1-R)e^{z/\xi_2}\right], \tag{2}$$

where I is the irradiance at z, R = 0.62, ξ_1 and ξ_2 are attenuation lengths equal to 1.5 and 20 m, respectively, and z is the vertical coordinate, positive upward with the origin at mean sea level.

[10] The model forcing also includes the net surface freshwater flux which is diagnosed from model results using the following approach due to the lack of observations. We first integrate the model with the surface freshwater flux set to zero. The transfer function (i.e., differences in magnitude in this study) between the modeled sea surface salinity, SSS_m, and observed sea surface salinity, SSS_o, at MB1 is determined, and then used to estimate the evapora-

Table 1. List of Four Numerical Experiments Forced by Different Combinations of Wind (W), Tides (T), and Buoyancy Forcing Associated With Sea Surface Heat and Freshwater Fluxes (B)

Name of Run	External Forcing	Temperature and Salinity
Exp-Control	W + T + B	non-uniform
Exp-Wind	W + B	non-uniform
Exp-Tide	T + B	non-uniform
Exp-Baro	W	uniform

tion minus precipitation $E\text{-}P = \frac{\Delta z}{SSS_o}\frac{\partial}{\partial t}(SSS_0 - SSS_m)$ to produce the time series shown in Figure 2d.

2.3. Model Forcings Along Open Boundaries

[11] Along the outer model open boundaries, the radiation condition of *Davies and Flather* [1978] is used:

$$U_B^n = U_p^n + \frac{c}{h}\left(\eta_B^n - \eta_t^n - \eta_r^n\right), \tag{3}$$

where U_B^n and η_B^n are the model-calculated normal flow and surface elevation at the open boundaries, U_p^n is a specified normal flow and set to be U_{B-1}^n for simplicity, c is the phase speed, h is the local water depth, η_t^n is the tidal elevation, and η_r^n represents the remotely generated waves. Superscript n indicates the time step, subscript B represents the boundary grid point, and $B - 1$ is the interior model grid point closest to the open boundary. Time series of η_t shown in Figure 2b is determined using the simplified incremental approach discussed by *Sheng and Wang* [2004] from the tidal sea level prediction at Lunenburg Harbour, which was made by the Canadian Hydrographic Service using more than 60 tidal constituents determined from historical sea level observations at the harbor. Time series of η_r in Figure 2b is determined from the observed non-tidal sea level at SB2 [*Zhai et al.*, 2007] using the same method. The normal flow along the open boundaries of the inner model is calculated by equation (3) with U_p^n, η_t^n and η_r^n taken from the outer model results and interpolated onto the inner model grid.

[12] Adaptive boundary conditions are used for temperature and salinity at the inner model open boundaries. It first uses an explicit *Orlanski* [1976] radiation condition to determine whether the open boundary of the inner model is passive (outward propagation) or active (inward propagation). If the open boundary is passive, the model temperature and salinity are radiated outward. If the open boundary is active, the inner model temperature and salinity at open boundaries are restored to the temperature and salinity calculated by the outer model and interpolated onto the inner model grid, with the restoring timescale set to 0.1 day.

[13] The model temperature and salinity at the outer model open boundaries are restored to the observed temperature and salinity at Station 2 on the inner Scotian Shelf (Figure 1) with different restoring timescales. Satellite observations of the sea surface temperature (not shown) suggest that bands of cool water existed off Halifax and along the western half of the shore from days 225 to 250, then gradually disappeared and the warm inner-shelf water moved toward the coast and extended southwestward from days 250 to 280. After day 280, bands of cold water occurred again along the coast. Therefore a longer restoring timescale of 10 days is used at the outer model open boundaries for the periods from days 225 to 250 and after day 280 to allow the model dynamics to generate the local upwelling in the bays. A shorter restoring timescale of 0.1 day is used from days 250 to 280 to approximate the influence of the above mentioned warming event on the inner Scotia Shelf.

3. An Upwelling-Downwelling Event in August 2003

[14] Observations suggest that water temperatures with periods of 1–10 days have strong spatial variability associated with wind-induced upwelling and downwelling [*Zhai et al.*, 2007]. Here, an examination of such events is made using the inner model results when the nested-grid modeling system is driven by the complete suite of forcings, referred to as the "control" run (Exp-Control, Table 1). Three additional model experiments (Table 1) were also conducted to isolate the dynamical influences of wind, tides, and baroclinic effects on the circulation and temperature fields. The nested-grid modeling system is forced by the wind and buoyancy forcing in the first additional experiment (Exp-Wind), and by the tide and buoyancy forcing in the second experiment (Exp-Tide). In the third experiment referred to as the barotropic run (Exp-Baro), the modeling system is forced by wind only, and temperature and salinity are set to be uniform. Other model parameters are the same as in the control run. All model runs are integrated from days 224 to 299, 2003, and here we focus on the model results from days 234 to 237 during which temperature and salinity have significant spatial variations.

3.1. Circulation

[15] The near-surface (1.5 m) and sub-surface (7.5 m) currents and temperatures shown in Figures 3a–3c and 4a–4c are those produced by the inner model in the control run at 0000 UTC 22 August (day 234.0), 1424 UTC 23 August (day 235.6), and 1912 UTC 25 August (day 237.8) 2003, respectively. The local wind stress at day 234.0 is northeastward with a magnitude of ~0.1 Pa. The simulated near-surface currents at this time (Figure 3a) are nearly northeastward over the deep water region to the east of LB and Rose Bay (RB), and asymmetric inside LB in the sense that the southeastward currents are stronger over northern LB than those over southern LB. The strong ebb tidal jet is evident exiting Corkum's Channel. The simulated sub-surface currents at this time (Figure 4a) are nearly northward outside LB, and are relatively weak inside LB. A comparison of the model-calculated currents from the three additional numerical experiments (Figures 3–4d, 3–4j and 3–4g) shows that the coastal currents in the control run are mainly forced by wind, whereas the jet-like flows through Corkum's Channel and over eastern East Point Island are largely generated by the tidal forcing. Baroclinicity plays an important role in generating the asymmetry of the wind-driven currents in LB shown in Figures 3a and 3d, as discussed by *Zhai et al.* [2008].

[16] By day 235.6 the wind stress has changed to southeastward with an amplitude of ~0.1 Pa. There is a strong and nearly southward throughflow over the deep water region outside LB at this time in the control run

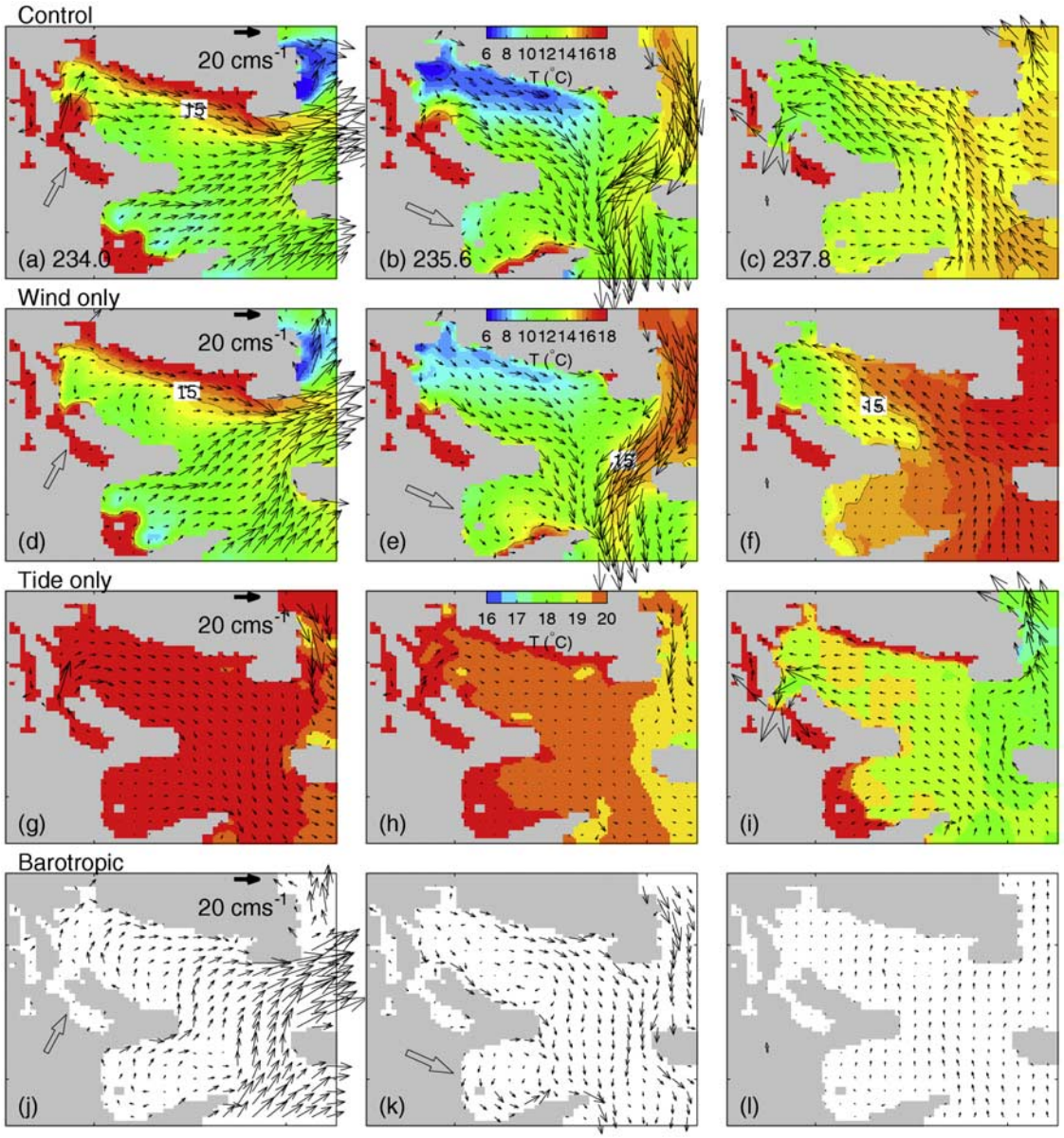

Figure 3. Near-surface (1.5 m) currents and temperatures at days (a) 234.0, (b) 235.6, and (c) 237.8 produced by the inner model in the control run; (d–f) from the experiment forced by wind only (Exp-Wind); (g–i) from the experiment forced by tides only (Exp-Tide); (j–l) from the experiment forced by wind only with temperature and salinity set to be constant (Exp-Baro). Open arrows denote wind stress. Velocity vectors are plotted at every fourth model grid point.

(Figure 3b). The currents inside LB flow southeastward, and veer southward on reaching the deep water region. The currents near southern East Point Island are relatively weak. The sub-surface currents (Figure 4b) are characterized by compensating return flow inside LB and southward throughflow east of EPI and in the region of deeper water outside LB. A comparison of model-calculated currents from the three additional experiments (Figures 3–4e, 3–4h and 3–4k) shows that the throughflow in the control run at this time is strongly affected by the baroclinicity, and that baroclinic effects enhance the subsurface return flow over southern LB. The tidally forced currents are relatively weak in LB at this time.

[17] The wind stress has relaxed almost completely by day 237.8. At this time, the near-surface currents in the control run (Figure 3c) flow northward over the deep water region, and veer northwestward when entering the bay. There are strong southwestward inflows through Corkum's Channel, indicative of the incoming tide. The sub-surface flow at this time (Figure 4c) is dominated by the incoming tidal flow over northern LB, with much weaker flows over southern LB where the wind-forcing-only case shows a relatively strong southeastward flow. A comparison of model-calculated currents in the four experiments (Figures 3f, 3i and 3l) demonstrates that the near-surface northwestward flow in LB in the control run at day 237.8 is strongly affected by the wind-induced baroclinic circu-

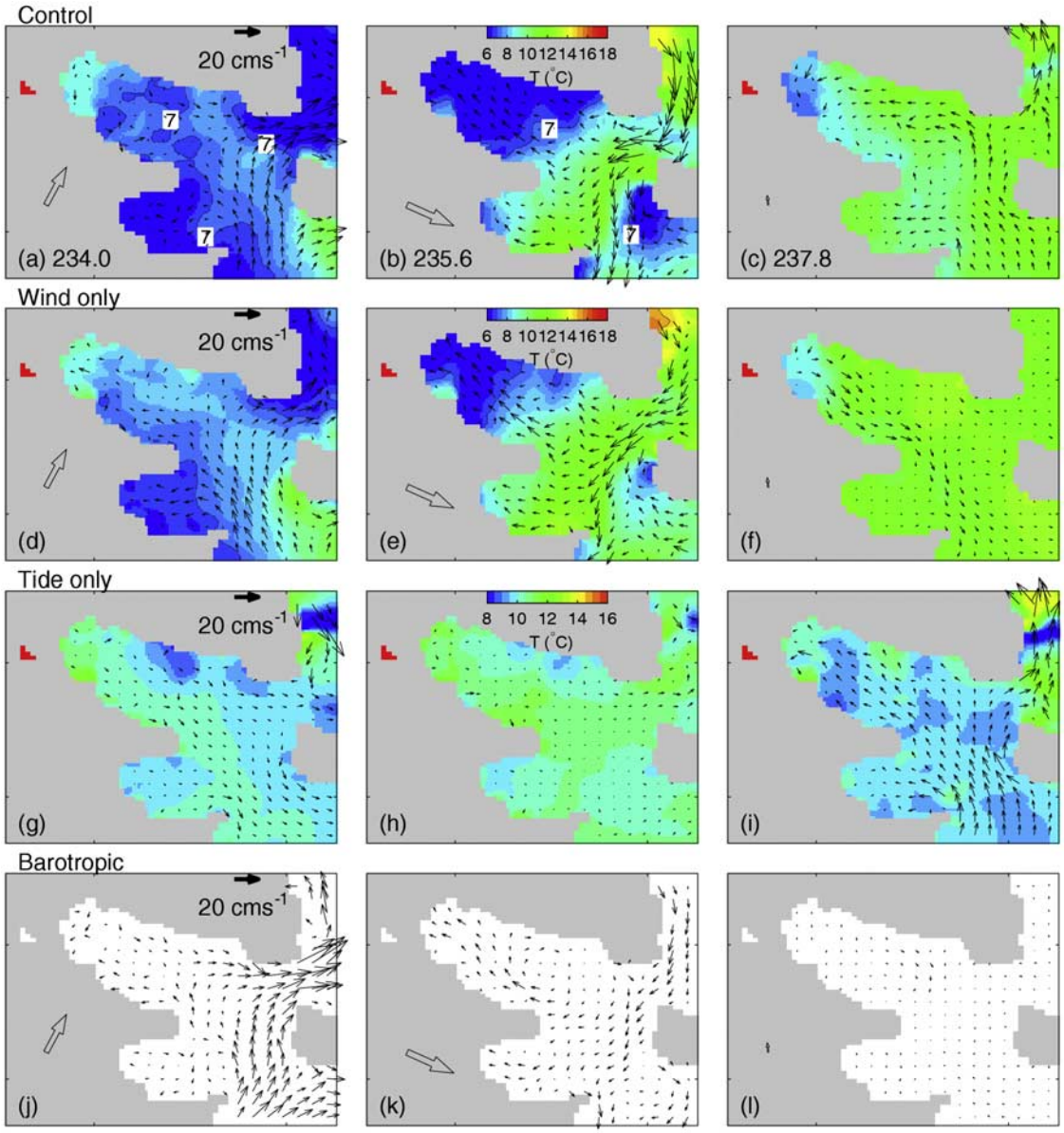

Figure 4. Sub-surface (7.5 m) currents and temperatures at days (a) 234, (b) 235.6 and (c) 237.8 produced by the inner model in the control run; (d–f) from the experiment forced by wind only (Exp-Wind); (g–i) from the experiment forced by tides only (Exp-Tide); (j–l) from the experiment forced by wind only with temperature and salinity set to be constant (Exp-Baro). Open arrows denote wind stress. Velocity vectors are plotted at every fourth model grid point.

lation, associated with the propagation of baroclinic waves excited by the wind-forcing at earlier times, [*Zhai et al.*, 2008].

3.2. Temperature

[18] The temperature fields produced by the inner model shown in Figures 3 and 4 demonstrate that the three-dimensional circulation plays a significant role in generating the spatial variability of temperatures in LB, since the surface heat flux used to drive the modeling system in this study is spatially uniform (apart from the relatively weak restoring term in equation (1)). The simulated near-surface (1.5 m) temperatures on day 234.0 in the control run (Figure 3a) are characterized by relatively cold water of about 12°C over the deep water region to the south of LB and east of RB. The colder (warmer) water of less (greater) than 15°C over southern (northern) LB at this time are caused by wind-induced local upwelling (downwelling). The water temperatures are above 15°C in the two coves and southwestern RB due mainly to the shallow topography. The simulated sub-surface (7.5 m) temperatures in the control run at this time (Figure 4a) are relatively cold and below 7°C in RB and over eastern LB associated mainly with local upwelling and horizontal advection. There is relatively warm water over inner LB associated with the shallow local topography. A comparison of the model-calculated temperatures from the two additional, baroclinic numerical experiments (Figures 3–4d and 3–4g) shows that

Table 2. Comparison of Observed and Simulated Tidal Elevations at Five Sites in Lunenburg Bay and Adjacent Two Coves[a]

	Amplitude, cm			Phase, deg		
Station	Observed	Modeled	ΔH	Observed	Modeled	$\Delta\phi$
			M_2			
SB2	62.29	62.21	0.08	197.27	198.22	−2.09
SB3	61.47	61.94	−0.47	197.10	198.21	−1.11
H	62.46	62.23	0.23	194.71	198.23	−3.52
B	60.67	61.95	−1.28	197.73	200.84	−3.11
M	44.21	44.26	−0.05	232.54	244.94	−12.40
			S_2			
SB2	16.22	16.82	−0.60	26.72	13.33	13.39
SB3	16.06	16.75	−0.69	26.78	13.35	13.43
H	16.15	16.81	−0.66	24.21	13.31	11.00
B	15.92	16.63	−0.71	31.09	16.65	14.44
M	9.89	10.42	−0.53	69.70	73.44	−3.74
			N_2			
SB2	13.82	13.93	−0.11	50.87	56.62	−5.75
SB3	13.55	13.88	−0.33	49.93	56.65	−6.72
H	14.09	13.94	0.15	48.69	56.63	−7.94
B	13.08	13.83	−0.75	54.66	59.49	−4.83
M	9.84	10.42	−0.58	95.82	73.44	22.38

[a]In the Table, ΔH and $\Delta\phi$ represent model errors in simulating amplitudes and phases.

the spatial pattern of near−surface temperatures is mainly generated by wind-forcing, except that the warm temperature front at the mouth of Corkum's Channel is advected northeastward by the strong tidal jet compared to the run with wind-forcing only (Exp-Wind). With tidal forcing only (Exp-Tide), the temperature fields are nearly horizontally uniform at the surface (Figure 3g), and have weak horizontal variation at sub-surface depth due to the interaction of topography and the thermocline (Figure 4g).

[19] The simulated near-surface temperature on day 235.6 in the control run (Figure 3b) is characterized by relatively warm water over the deep water region outside LB, due to the southward advection of warm water from MB. The near-surface temperature has a large difference of about 5°C between northern LB and southern LB, associated with local wind-induced upwelling and downwelling. The coastal water in the two coves is relatively warm. The simulated sub-surface temperature in the control run at this time (Figure 4b) is nearly uniform and colder than 7°C inside LB. The sub-surface temperature is relatively warm at the entrance of LB due to the advection of warm water from southern MB. A comparison of model-calculated temperatures from the additional numerical experiments (Figures 3–4e and 3–4h) shows that the spatial pattern of temperature in the control run is similar to that forced by wind only (Exp-Wind). However, without tidal forcing, the temperatures forced by wind alone tend to be warmer than those in the control run.

[20] By day 237.8, the simulated near-surface temperature in the control run (Figure 3c) is warmer over the deep water region outside LB than in Figure 3b. At this time, the near-surface temperature inside LB has a weak spatial variation with relatively warm water on the northern side of the bay, due mainly to the propagation of baroclinic waves from southern MB into LB, which carry downwelling signals and switch off the local upwelling in the bay (*Zhai et al.*, 2008).

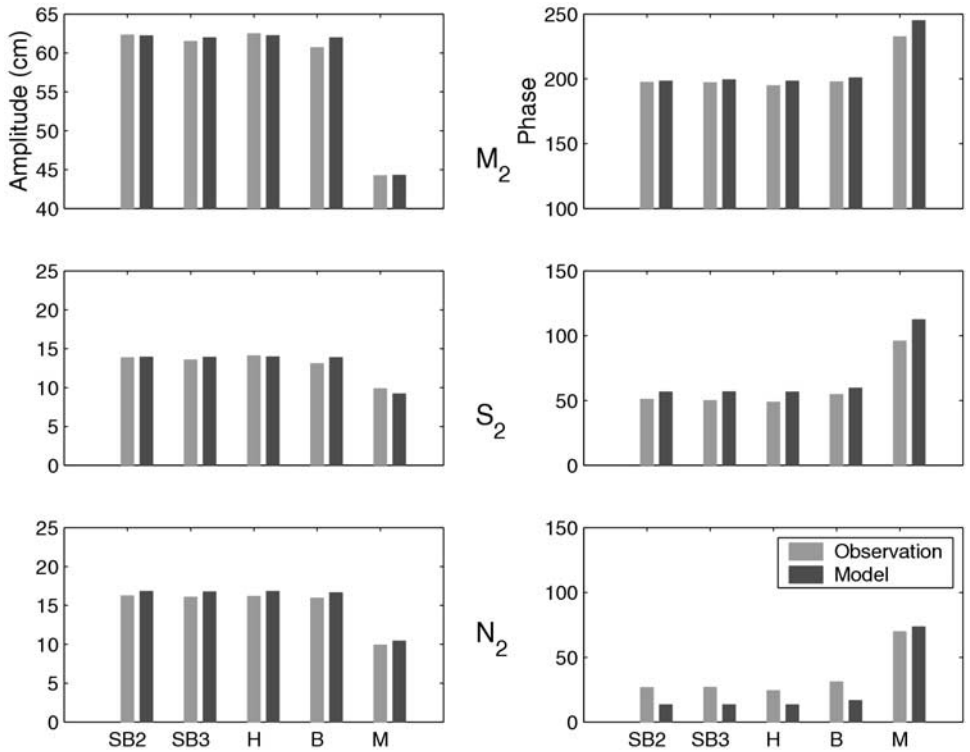

Figure 5. Comparison of observed and model calculated amplitudes and phases of M_2, S_2 and N_2 constituents of tidal elevations at sites SB2, SB3, and H in Lunenburg Bay, at site B in Lower South Cove, and at site M in Upper South Cove respectively.

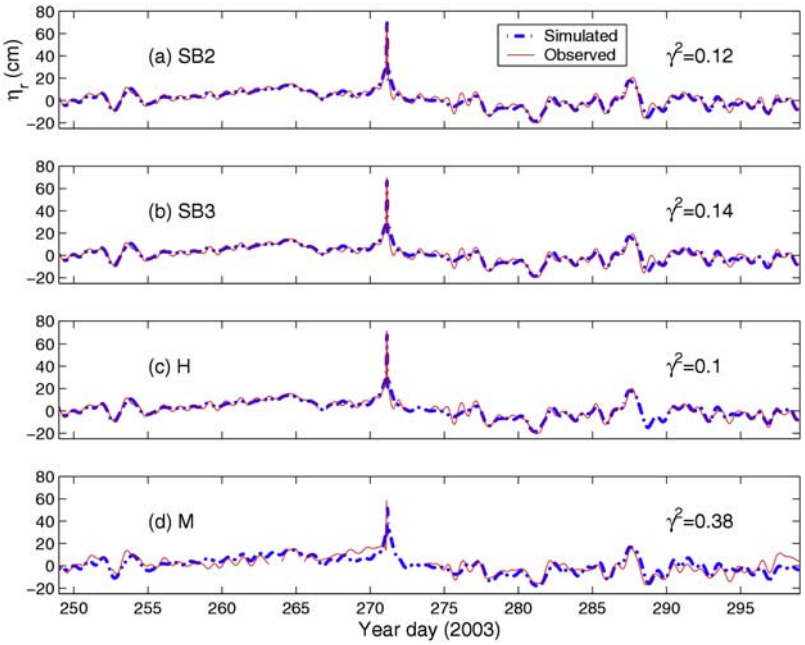

Figure 6. Comparison of observed and simulated non-tidal elevations at sites (a) SB2, (b) SB3, (c) H in Lunenburg Bay, and at site (d) M in Upper South Cove. The simulated results are produced by the nested-grid inner model in the control run.

The cold temperature front is being advected southwestward through Corkum's Channel into two coves by the incoming tide. The sub-surface temperature is nearly uniform and about 10°C over the study region. A comparison of model-calculated temperatures from the two baroclinic experiments shown in Figures 3–4f and 3–4i shows that the spatial pattern of temperatures in the control run is generated by the wind and tidal forcing. In the absence of tidal advection and mixing, temperatures forced by wind only (Figures 3g, 3h and 3i) tend to be warmer than those in the control run. Temperatures forced by tides only (Figures 3d, 3e and 3f) are patchy, implying the interaction of flood tidal currents and topography.

4. Assessing the Model Performance

[21] The hindcast skill of the nested-grid modeling system is examined by comparing the inner model results in the

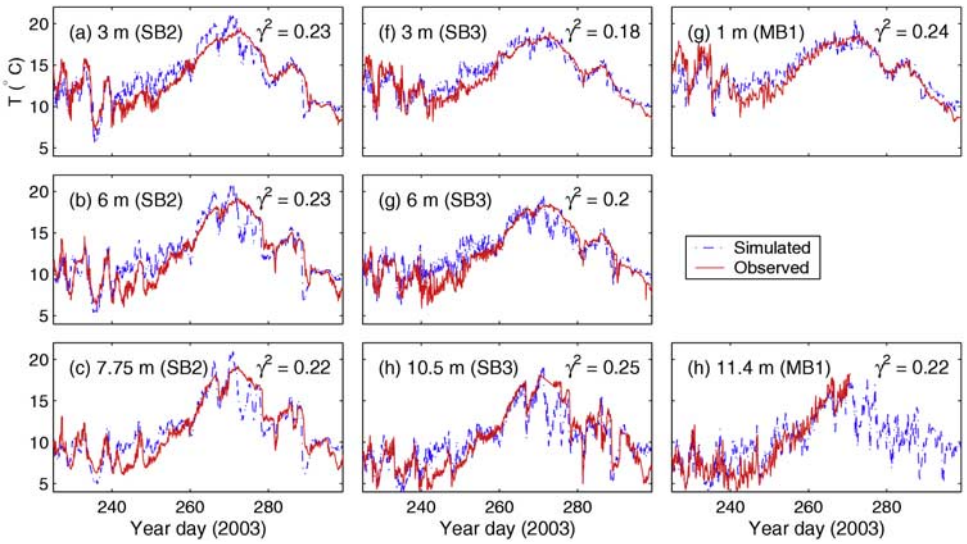

Figure 7. Comparison of observed and simulated temperatures at depths of 3, 6, and 7.5 m at site SB2 (left panels); at depths of 3, 6, and 10.5 m at site SB3 (middle panels), and at depths of 1, 11.4 m at site MB1 (right panels). The simulated results are produced by the nested-grid inner model in the control run.

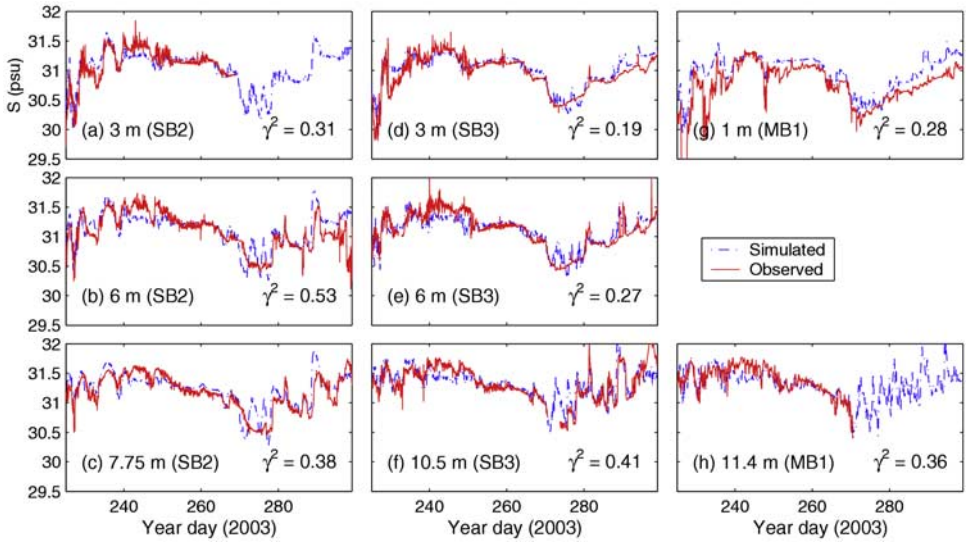

Figure 8. Comparison of observed and simulated salinities at depths of 3, 6, and 7.75 m at site SB2 (left panels); at depths of 3, 6, and 10.5 m at site SB3 (middle panels), and at depths of 1 and 11.4 m for site MB1 (right panels). The simulated results are produced by the nested-grid inner model in the control run.

control run with the observations made in LB during the study period. The model hindcast skill is quantified in terms of the γ^2 values defined as [*Thompson and Sheng*, 1997]:

$$\gamma^2 = \frac{Var(O-M)}{Var(O)}, \tag{4}$$

where O and M are the observed and model-calculated variables respectively, and *Var* is the variance, and all variables are sampled every half hour. The γ^2 value is a measure of the variance of the hindcast error upon the variance of the observations. The smaller γ^2 is, the better the model results fit the observations. It should be noted that γ^2 could be greater than unity. In the case of $\gamma^2 > 1$, the variance of the observations increases with the subtraction of the model results from the observations. In this study, $\gamma_c^2 = 1$ is used as a threshold value to access the model performance.

4.1. Surface Elevation

[22] To examine the model performance in simulating surface elevations in LB, the tidal and non-tidal components of simulated and observed sea levels at five locations in the bay are decomposed using the tidal analysis package developed by *Pawlowicz et al.* [2002]. The comparison of the three major constituents of semi-diurnal tidal elevations (M_2, N_2, and S_2) is shown in Table 2 and Figure 5. The differences between the simulated and observed amplitudes of the three major constituents are generally less than 1 cm. The differences in phases are generally less than 15° (0.5 hour). Both the observed and simulated elevations show that the tidal elevations are nearly spatially uniform at four stations in LB and at B in Lower South Cove. There is a significant reduction of semi-diurnal tidal elevations at M in USC, which is mainly associated with the hydraulic control and nonlinear tidal dynamics as discussed by *Sheng and Wang* [2004]. The tidal asymmetry produced by the inner model is determined by the volume of water going through

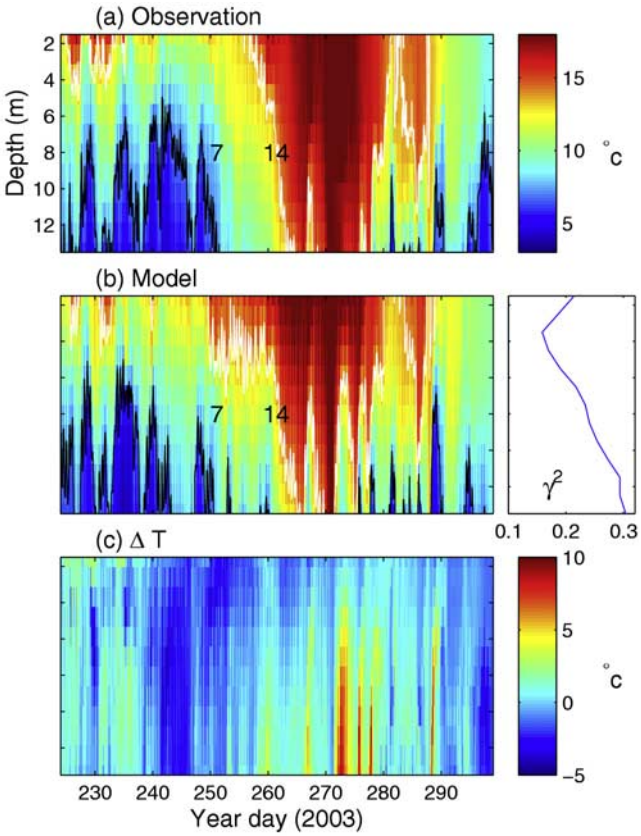

Figure 9. Time-depth distributions of (a) observed, (b) modeled, and (c) the difference, observed minus simulated temperatures at SB3. The observed temperatures were made by the minilog temperature recorders and the bottom pressure-temperature sensors at SB3. The simulated results are produced by the nested-grid inner model in the control run.

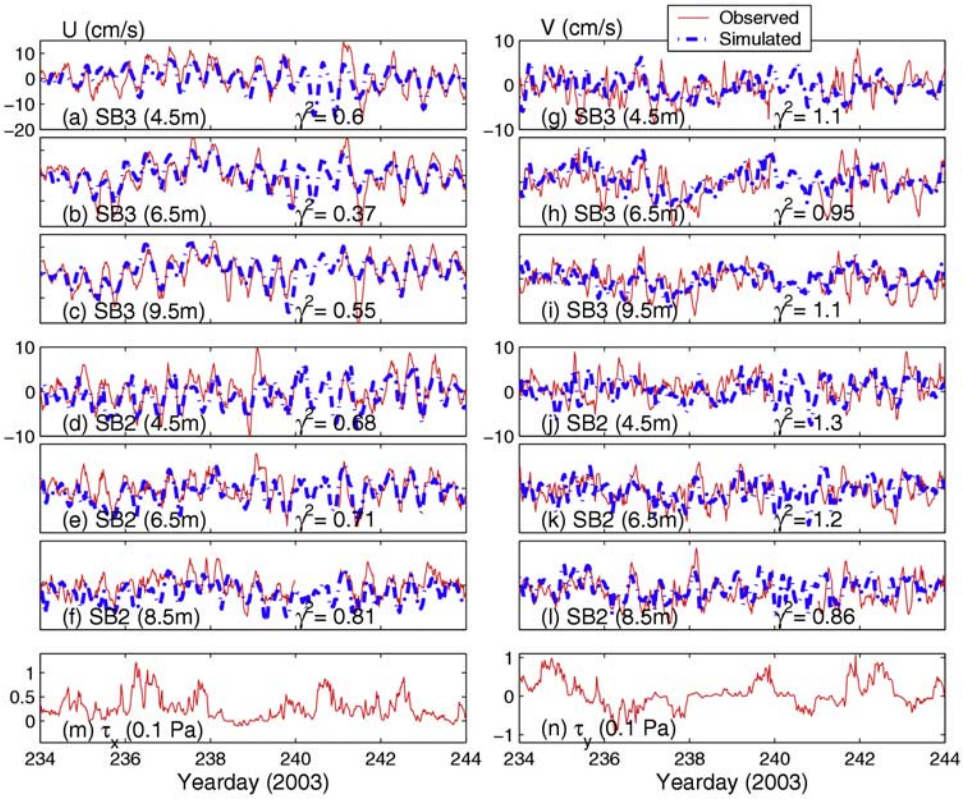

Figure 10. Comparison of eastward (left panels) and northward (right panels) components of observed and simulated currents at depths of 4.5, 6.5, and 9.5 m at site SB3 (left panels), and those at depths of 4.5, 6.5, and 8.5 m at site SB2 (right panels) from days 234 to 244, 2003. Bottom two panels are (m) the eastward and (n) northward wind stress.

the narrow mouth between the two coves. The fair agreement between the observed and simulated tidal elevations in USC indicates that the model reproduces reasonably well the volume transport of the tidal flow through the mouth, although the model does not resolve the detailed circulation features in the mouth and adjacent areas.

[23] The observed and simulated non-tidal sea levels are shown in Figure 6 (by "non-tidal" we mean the sea level with the tides removed). The time series in this figure demonstrate that the inner model in the control run captures the rapid changes in the non-tidal sea level associated with Hurricane Juan on 29 September 2003 (day 271), the major event in the time series. The γ^2 values are about 0.1 in LB and about 0.4 in USC, indicating that the inner model performs very well in simulating non-tidal sea levels in LB and fairly well in USC.

4.2. Temperature and Salinity

[24] Figures 7 and 8 demonstrate that the inner model in the control run reproduces the low-frequency variability (with periods of longer than 10 days) of the observed temperature and salinity at the three sites (SB2, SB3 and MB1) in LB. In addition, the inner model also captures the observed upwelling-downwelling events with periods of <10 days at the three sites. However, the simulated subsurface temperature and salinity between days 272 and 280 are about 5 °C lower and 0.5 psu higher than the observations respectively, indicating that the inner model overestimates the high-frequency variability (<10 days) after Hurricane Juan. The γ^2 values are typically less than 0.25 for temperature, and generally less than 0.4 for salinity, indicating that the inner model simulates reasonably well the observed temperature and salinity. Note that the large γ^2 value of 0.53 at 6-m depth at SB2 for salinity may be due to problems with the instrument around day 299.

[25] To further examine the model skill in simulating the vertical structure of temperatures at site SB3, the time-depth distribution of simulated temperatures in the control run are compared with the observed temperature made by minilog temperature recorders and pressure-temperature sensors at site SB3 (Figure 9). The inner model captures the dominant features of the evolving thermal stratification. The water column at the site is strongly stratified in August (days 213 to 243), becomes weakly stratified in September (days 244–273), and restratifies again in October (days 274–304). There are strong isotherm displacements with periods of several days during the first 25 days. The 7°C isotherm rises by about 7 m, then returns to its original depth over several days, as a consequence of wind-induced upwelling and downwelling, and propagation of baroclinic waves. In the middle of the record, there is a downward displacement of the 14°C isotherm. This is followed by a fairly steady rise of the temperature throughout the water column until day 280. As described in section 5, this is due to a combination of net surface heat input and advection of warm water into the bay. On 29 September (day 271), the temperature of the whole

Table 3. A Comparison of Observed and Simulated M_2 Tidal Current Ellipses Parameters at Three Different Depths of Sites SB2, SB3, and MB1 in Lunenburg Bay

	Semi-major, cm		Orientation, deg		Phase, deg	
Station	Observed	Modeled	Observed	Modeled	Observed	Modeled
SB2 (3.5m)	2.49	2.61	176.87	174.28	130.92	157.18
SB2 (5.5m)	2.43	2.20	165.57	171.87	116.21	135.23
SB2 (7.5m)	1.91	1.78	160.25	152.84	101.26	134.42
SB3 (3.5m)	3.86	4.39	157.94	160.89	140.65	156.42
SB3 (6.5m)	4.29	4.04	158.49	165.49	125.43	134.90
SB3 (10.5m)	5.11	3.98	162.51	168.48	118.49	105.11
MB1 (3.5m)	4.07	5.00	135.36	136.25	97.18	104.36
MB1 (6.5m)	4.25	4.17	139.62	139.63	94.70	101.85
MB1 (10.5m)	2.80	1.63	165.58	168.05	70.45	80.37

water column reaches 18°C and is well-mixed in association with the strong vertical mixing induced by Hurricane Juan. Before the end of the record, the 7°C isotherm reappears due to local upwelling and advection of cold water into the bay.

[26] Figure 9c shows the difference, observed minus simulated temperatures at SB3. There are warm biases of ~2°C from days 240–250 and cold biases of ~5°C below 5 m depth from days 272–280 after Hurricane Juan in the model temperatures. Both of these seem likely to be associated with the model open boundary conditions. The γ^2 values, also shown in the figure, are less than 0.3, but have a tendency to increase with depth, probably due to the specification of temperature along the model open boundaries. A sensitivity study shows that the model results at SB3 are sensitive to changes in open boundary conditions (not shown). Further improvement of the open boundary conditions can be done by using a three-level nesting or data assimilation technique, but is not pursued further in this study.

4.3. Currents

[27] We next assess the model hindcast skill in simulating the three-dimensional circulation in LB. Figure 10 shows the time series of observed and simulated currents at SB3 and SB2 from days 234 to 244 when there are relatively large baroclinic effects as shown in Figures 3 and 4. The inner model in the control run captures the general features of the circulation, that is both the semi-diurnal tidal currents and the non-tidal currents. From days 234–236, when the wind stress is roughly northward, the simulated sub-surface non-tidal currents at SB3 are characterized by northwestward inflow of ~5 cm s^{-1} (see also Figure 4). From days 236–238 when the wind stress is roughly eastward, there is approximately eastward non-tidal outflow of ~5 cm s^{-1} at SB3, and from days 238–240 when the wind dies down, the non-tidal currents are characterized by weak northwestward return flow at SB3. The γ^2 values typically range from 0.4 to 0.8 for the eastward component, and from 0.9 to 1.3 for the northward component. Generally speaking, the model does better just below the surface and with along-bay rather than cross-bay currents.

[28] Tidal analyses of the observed and simulated currents (Table 3 and Figure 11) indicate that the M_2 tidal flow explains more than 50% of the total variance of tidal currents at sites SB2, SB3 and MB1, which is consistent with the previous findings of *Sheng and Wang* [2004]. The inner model reproduces reasonably well the characteristics of the observed M_2 tidal current ellipses. Note that the semi-minor axes have large analysis errors since the signal-to-noise ratio (defined as the square of the ratio of amplitude to amplitude error) is smaller than one. The M_2 tidal currents are nearly rectilinear and aligned roughly with the bottom topography at sites SB3 and MB1, but have relatively large ellipticity at SB2 due mainly to the influence of the jet-like flow through Corkum's Channel. The semi-major axes of M_2 tidal current ellipses reduce near the bottom at sites SB2 and MB1, likely due to bottom friction. There is generally good agreement between the simulated and observed semi-major axes at the three sites, but relatively large errors at 10.5-m depth at SB3 and MB1, probably due to the less

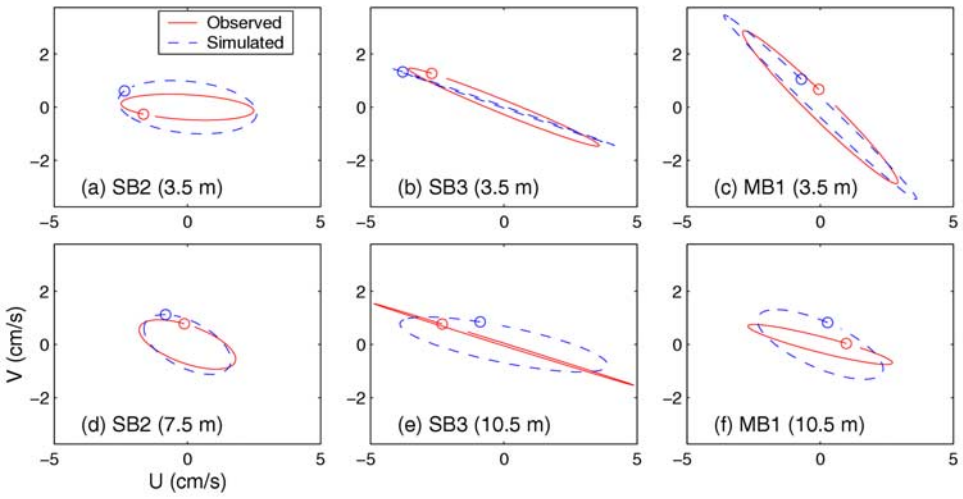

Figure 11. Comparison of the observed and simulated M_2 tidal current ellipses at two different depths of (a, d) SB2, (b, e) SB3, and (c, f) MB1.

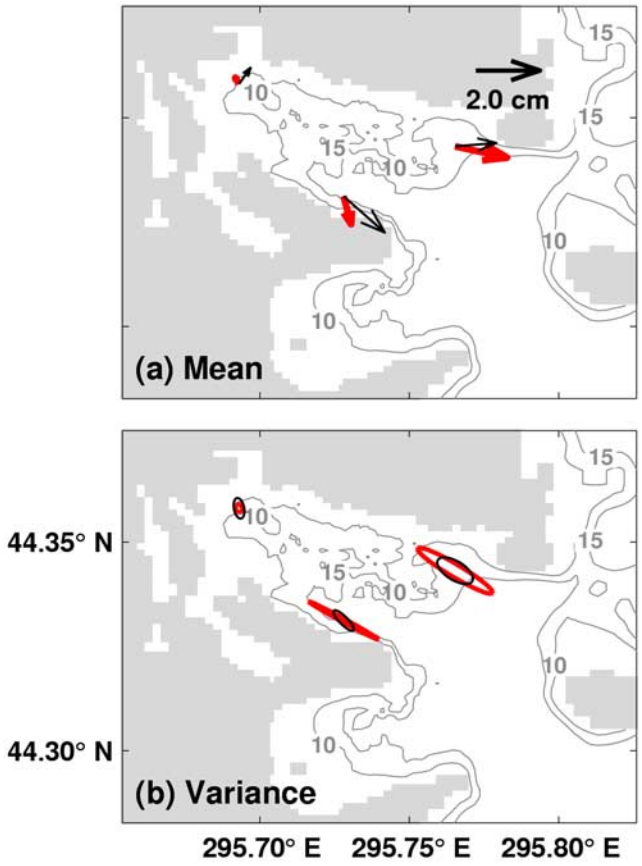

Figure 12. Comparison of observed (thick lines) and simulated (thin lines) (a) means and (b) variances of near-surface sub-tidal currents at 4.5 m at three sites from days 260 to 293, 2003.

accurate representation of the topography. The simulated orientations and phases of M_2 tidal current ellipses agree reasonably well with the observed ones at the three sites with errors typically less than 10°.

[29] To examine the model performance in simulating the horizontal structure of the currents at sub-tidal frequencies, the currents are low-pass filtered with a cutoff period of 27 h. Means and variances of the simulated sub-tidal currents are calculated at the three sites from days 260 to 293, and compared with observations (Figure 12). The simulated time mean current at 4.5 m (Figure 12a) is nearly eastward at MB1 and in the same direction as the observations. The simulated mean currents at SB3 and SB2 are aligned with the bottom topography and tend to be larger than in the observations. The major axes of variance of simulated sub-tidal currents at 4.5 m Figure 12b) are in the same direction as those of the observations, but have smaller magnitudes at SB2 and SB3, indicating that the nested-grid system underestimates the variances of observed near-surface currents during the period. Principal component analysis [*Emery and Thomson*, 1998] demonstrates that the first mode of the simulated and observed sub-tidal currents accounts for 43% and 47% of their variances respectively and shows similar spatial patterns (Figure 13). The eigenvector for the first mode (Figure 13a) shows oppositely directed currents at MB1 and SB3, indicating circulation around the bay in both the model and the observations. The comparison of the first mode coefficient (Figure 13b) indicates that the inner model captures the observed temporal variability, but reproduces a smaller amplitude during large wind events.

5. Heat and Salt Budgets

[30] One of the important features for the hydrography in coastal waters is the relative role of the local and nonlocal processes in determining the heat budget. Using the observations alone, *Zhai et al.* [2007] found evidence from the observations that advection associated with the first EOF mode shown in Figure 13 played an important role at low frequencies in the heat budget of LB. Using the model results in the control run, we are better able to quantify the role of advection and horizontal mixing. In this section, the depth-integrated heat and salt budgets are examined by using

$$\underbrace{\frac{\partial H}{\partial t}}_{A} = \underbrace{-\langle u\frac{\partial T}{\partial x}\rangle}_{B}\underbrace{-\langle v\frac{\partial T}{\partial y}\rangle}_{C}\underbrace{-\langle w\frac{\partial T}{\partial z}\rangle}_{D}\underbrace{+\frac{Q_{net}}{\rho_0 c_p}}_{E}\underbrace{+\langle\nabla_h\cdot(A_h\nabla_h T)\rangle}_{F} \tag{5}$$

$$\underbrace{\frac{\partial S}{\partial t}}_{A} = \underbrace{-\langle u\frac{\partial S}{\partial x}\rangle}_{B}\underbrace{-\langle v\frac{\partial S}{\partial y}\rangle}_{C}\underbrace{-\langle w\frac{\partial S}{\partial z}\rangle}_{D}\underbrace{+SSS_0(E-P)}_{E}\underbrace{+\langle\nabla_h\cdot(A_h\nabla_h S)\rangle}_{F} \tag{6}$$

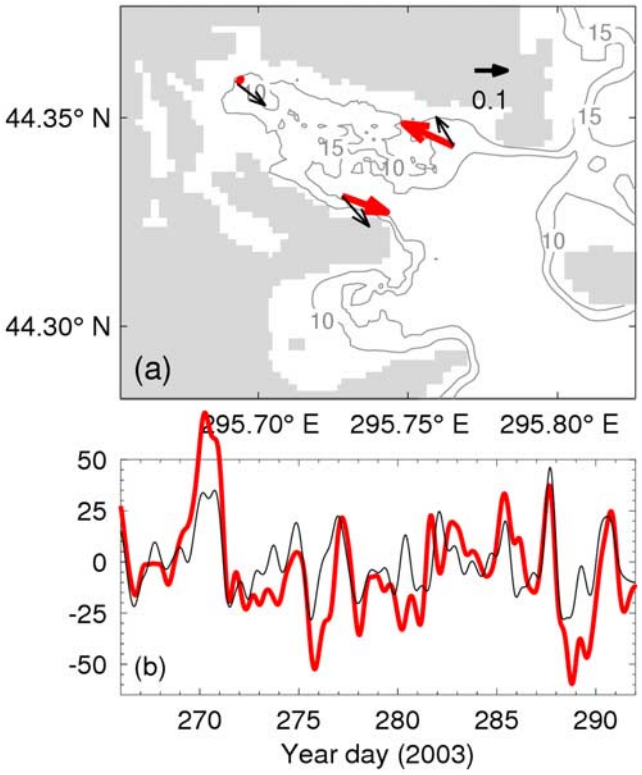

Figure 13. Principal component analysis of observed and simulated sub-tidal currents at 4.5 m: (a) the first EOF mode eigenvectors, (b) the first EOF mode coefficient of observed (thick lines) and simulated (thin lines) currents at three sites.

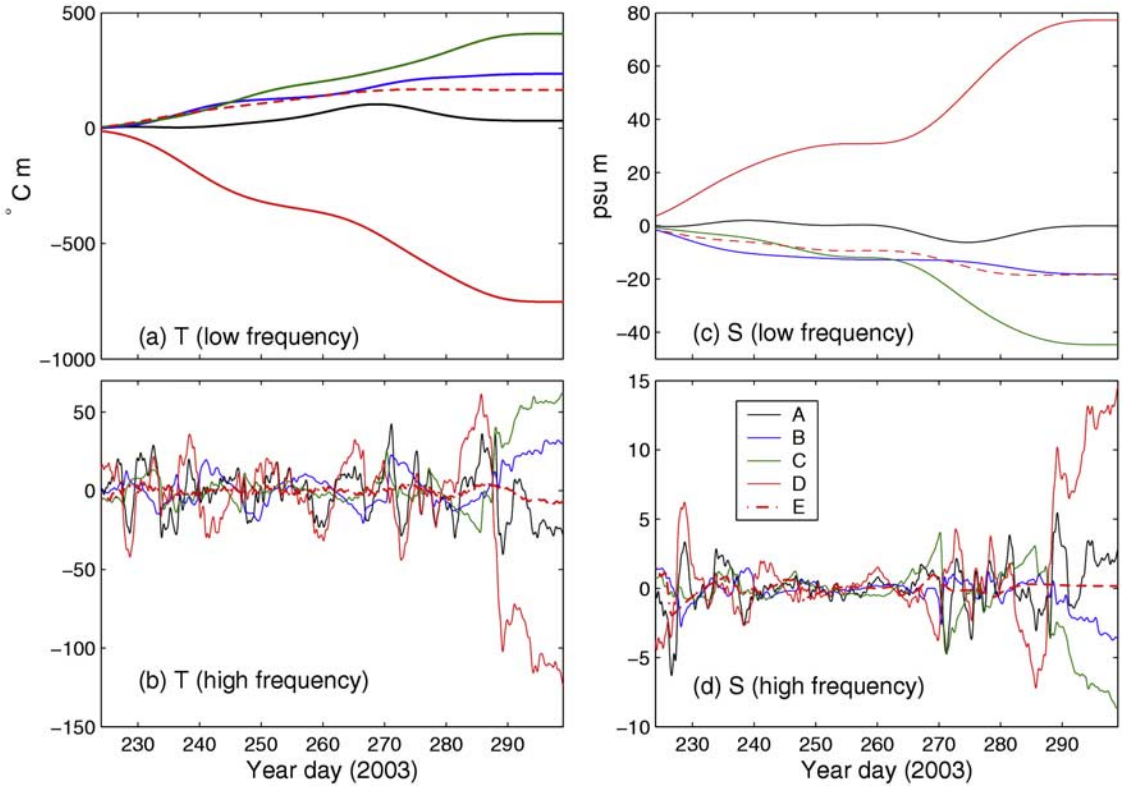

Figure 14. Time series of (a) the low-frequency and (b) high-frequency heat budgets, and (c) low-frequency and (d) high-frequency salt budgets at site SB3. Time-integrated heat (salt) content (A) is indicated by the black line, the eastward (B), northward (C) and vertical (D) advections by the blue, green and red lines, and the surface heating (E) by the dashed red line.

where $H = \int_{-h}^{0} Tdz$ is the local heat content stored in the whole water column, $\langle\rangle = \int_{-h}^{0} dz$, T is the model temperature, Q_{net} is the net surface heat flux, ρ_0 is the reference water density, c_p is the specific heat of water, u, v, w are the eastern, northern and vertical components of the model velocity, A_h is the horizontal eddy diffusivity coefficient, and $\nabla_h = (\frac{\partial}{\partial x}, \frac{\partial}{\partial y})$. The nonlocal processes associated with horizontal and vertical advection and horizontal mixing are represented by terms B-D and F on the right hand side of equations (5) and (6). The time-integrated heat balance at SB3 is discussed below in two frequency bands by filtering the terms in (5) and (6): a low-frequency band with periods of >30 days and a high-frequency band with periods of 1–30 days. The change in the heat content due to the horizontal mixing in the model is small and is not discussed further.

[31] The time-integrated heat and salt budgets in the low frequency band are shown in Figure 14. The balances at the end of the time series indicate the relative contributions of each term integrated over the study period. The heat budget during the study period (Figure 14a) is dominated by cooling of the water column due to vertical advection (∼−750°C m, red curve), i.e., upwelling, and warming due to horizontal advection (∼600°C m, green and blue curves) and surface heat input (∼170°C m). The same basic balance also applies to the salinity budget (Figure 14b). In this case, on average, salty water (∼80 psu m) is upwelled, tending to increase the salinity of the water column, while horizontal advection (∼−60 psu m) and the surface flux (∼−20 psu m) act to freshen the water column. It is noticeable that during a warming period in September (days 255–273, see Figure 9), cooling due to vertical advection is reduced, while horizontal advection continues to play a role in warming the water column. This is consistent with *Zhai et al.* [2007], who noted that the role played by advection is associated with the first EOF mode of the observed subtidal currents at the mooring sites SB3 and MB1 during this time.

[32] The heat balance in the high-frequency band (Figures 14b and 14d), however, shows that changes in the local heat (salt) content of the water column are associated mostly with vertical advection (i.e., upwelling/downwelling), and with horizontal advection acting oppositely but not dominating. This picture is confirmed by the correlations of advection terms B-D with the local heat content (term A). These take values of −0.26, −0.30, 0.62, respectively, indicating that the temporal variability of the local heat content is induced largely by vertical advection, with some contribution from the horizontal advection (all these correlations are statistically significant at the 1% level). A similar picture emerges for the salt budget. The correlations of terms B-D with the local salt content (term A) are −0.40, −0.21, and 0.56 respectively, indicating that the temporal variability of the local salt content is induced

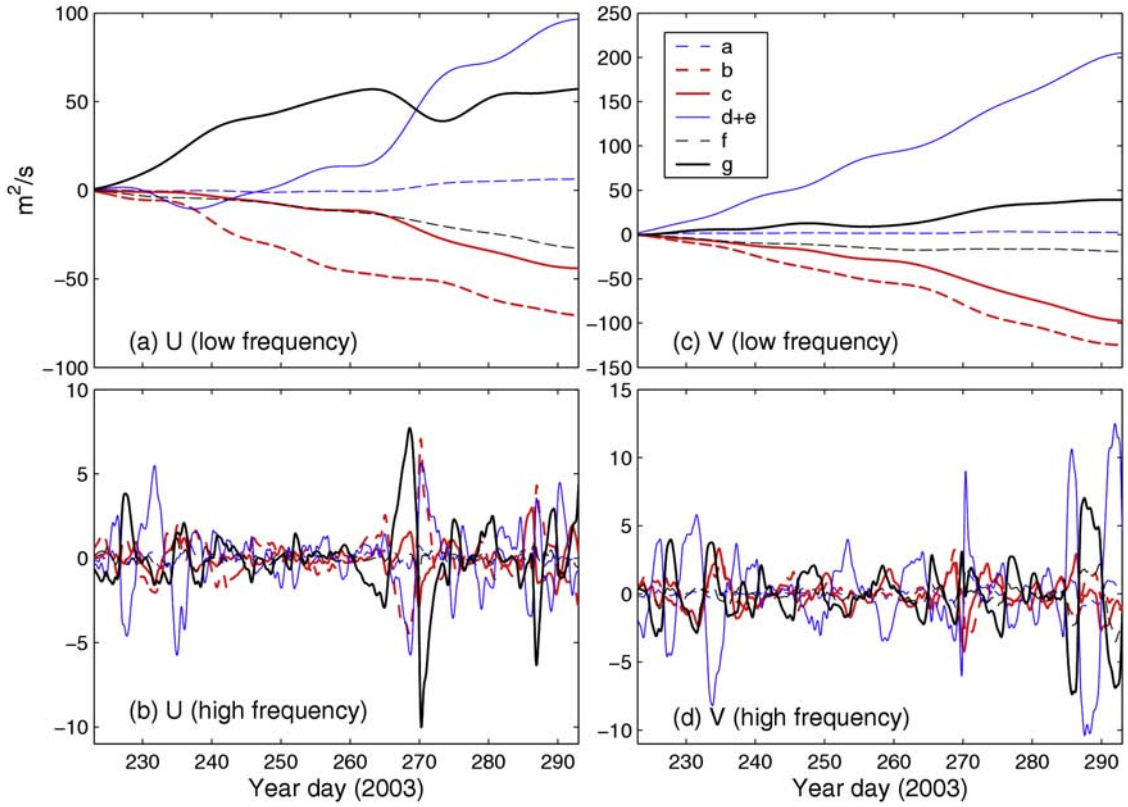

Figure 15. Time series of (a) low-frequency and (b) high-frequency momentum balances in the east direction, and (c) low-frequency and (d) high-frequency in the northward direction. The local acceleration term is indicated by the dashed blue line, the advection term by the dashed red line, the Coriolis term by the red line, the pressure gradient term by the blue line, the horizontal mixing term by the dashed black line, and the difference between surface wind stress and bottom friction by the black line.

largely by the vertical advection, with some contribution from horizontal advection.

6. The Depth-Integrated Momentum Balance

[33] We also perform an analysis of the depth-integrated momentum balance including the effect of stratification using the depth-integrated momentum equations defined as

$$\underbrace{\frac{\partial\langle u\rangle}{\partial t}}_{a} = \underbrace{-\langle\vec{u}\cdot\nabla u\rangle}_{b} \underbrace{+\langle fv\rangle}_{c} \underbrace{-\langle g\frac{\partial\eta}{\partial x}\rangle}_{d} \underbrace{-\langle\frac{1}{\rho_o}\frac{\partial P_b}{\partial x}\rangle}_{e} \underbrace{+\langle\nabla_h\cdot(A_m\nabla_h u)\rangle}_{f} \underbrace{+\langle\frac{\tau_x^s-\tau_x^b}{\rho_0}\rangle}_{g} \quad (7)$$

$$\underbrace{\frac{\partial\langle v\rangle}{\partial t}}_{a} = \underbrace{-\langle\vec{u}\cdot\nabla v\rangle}_{b} \underbrace{-\langle fu\rangle}_{c} \underbrace{-\langle g\frac{\partial\eta}{\partial y}\rangle}_{d} \underbrace{-\langle\frac{1}{\rho_o}\frac{\partial P_b}{\partial y}\rangle}_{e} \underbrace{+\langle\nabla_h\cdot(A_m\nabla_h v)\rangle}_{f} \underbrace{+\langle\frac{\tau_y^s-\tau_y^b}{\rho_0}\rangle}_{g} \quad (8)$$

where $P_b = g\int_z^0 \rho\, dz'$ is the density-driven internal pressure, and (τ_x^s, τ_y^s) and (τ_x^b, τ_y^b) are the eastward and northward components of surface wind and bottom stresses respectively. Other symbols in (7) and (8) are defined in the Appendix. As in the previous section for the heat budget, here the time-integrated momentum balances at SB3 are also discussed for the high and low frequency bands.

[34] At low frequencies (Figures 15a and 15c), the Coriolis (red) and momentum advection terms (dashed red) play an important role and effectively balance the combined effect of the surface minus bottom stress (black) and the pressure gradient term (blue), suggesting a modified geostrophic balance. By contrast, at high frequencies (Figures 15b and 15d), the dominant balance is between the wind minus the bottom stress (black) and the combined pressure gradient (blue), although the momentum advection and Coriolis terms do sometimes make a contribution. Repeating the analysis, but using the model results with the uniform temperature and salinity experiment (Exp-Baro) leads to similar results at both low and high frequency for the eastward (u) momentum equation, but reveals differences at low frequency for the northward (v) momentum equation. The latter is associated with the fact that the mean flow at SB3 is in the opposite direction in the control run

with stratification, compared to the barotropic run, and an issue to be discussed further in a later paper.

7. Summary and Discussion

[35] Forced by tides, surface wind stress, remotely generated waves, net surface heat flux and diagnosed surface freshwater flux, the nested-grid ocean circulation modeling system simulates the circulation and thermal structure in Lunenburg Bay (LB) in the summer and fall of 2003. The spatial and temporal variability of the simulated temperature and salinity is mainly associated with the wind-induced upwelling and downwelling, with some contribution from tidal advection and surface fluxes. The simulated currents show a strong baroclinic throughflow over the deep water region outside Lunenburg Bay that shows day-to-day variations associated with the wind. It should be noted that the superposition of model currents in experiments Exp-Wind and Exp-Tide differs from those in the control run during storm events (not shown), indicative of the nonlinear interaction between the tidal and wind-driven currents as discussed by *Wang et al.* [2007].

[36] The agreement between the simulated and observed surface elevations in the control run indicates that the inner model of the nested-grid system reproduces very well the observed surface elevations at 5 locations in the study region. The inner model also captures the observed variations of temperature and salinity at three sites in LB. The simulated semi-diurnal M_2 tidal current ellipses compare reasonably well with those derived from the observations, with the misfits generally smaller than 1 cm s^{-1} at the three sites. The inner model reproduces the temporal variability and spatial pattern of the first EOF mode of the observed subtidal currents, but underestimates the amplitude of the first mode coefficient during strong wind events.

[37] Based on the agreement between the simulated and observed fields, the model results in the control run are used to estimate the heat, salt and momentum balances at SB3. At low frequency (timescales larger than 30 days), the local heat and salt balance is dominated by cooling (increasing saltiness) due to vertical advection and warming (freshening) due to horizontal advection and the surface heat (freshwater) input. In the high-frequency band (timescales shorter than 30 days), the changes in local heat (salt) content are mainly controlled by vertical advection, indicating the effects of local upwelling and downwelling. The depth-integrated momentum balance in the low frequency band suggests a modified geostrophic balance, but with wind minus bottom stress and also advection playing a role. The momentum balance in the high-frequency band is dominated by the pressure term and the wind minus bottom stress.

Appendix A: The CANDIE Model

[38] The governing equations used in the CANDIE model are the same as those considered by *Sheng and Wang* [2004]. To facilitate physical interpretation, the equations are expressed in Cartesian coordinates

$$\frac{\partial u}{\partial t}+\nabla\cdot(\vec{u}u)-fv=-\frac{1}{\rho_0}\frac{\partial p}{\partial x}+\frac{\partial}{\partial z}\left(K_m\frac{\partial u}{\partial z}\right)+\nabla_h\cdot(A_m\nabla_h u), \tag{A1}$$

$$\frac{\partial v}{\partial t}+\nabla\cdot(\vec{u}v)+fu=-\frac{1}{\rho_0}\frac{\partial p}{\partial y}+\frac{\partial}{\partial z}\left(K_m\frac{\partial v}{\partial z}\right)+\nabla_h\cdot(A_m\nabla_h v), \tag{A2}$$

$$\nabla\cdot\vec{u}=0, \tag{A3}$$

$$\frac{\partial T}{\partial t}+\nabla\cdot(\vec{u}T)=\frac{\partial}{\partial z}\left(K_h\frac{\partial T}{\partial z}\right)+\nabla_h\cdot(A_h\nabla_h T), \tag{A4}$$

$$\frac{\partial S}{\partial t}+\nabla\cdot(\vec{u}S)=\frac{\partial}{\partial z}\left(K_h\frac{\partial S}{\partial z}\right)+\nabla_h\cdot(A_h\nabla_h S), \tag{A5}$$

$$\rho=\rho(T,S,p), \tag{A6}$$

$$p=g\int_z^\eta \rho dz, \tag{A7}$$

$$\frac{\partial\eta}{\partial t}=-\frac{\partial}{\partial x}\int_{-h}^{\eta}udz-\frac{\partial}{\partial y}\int_{-h}^{\eta}vdz, \tag{A8}$$

where u, v, w are eastward, northward, and vertical components of the velocity vector $\vec{u}$, respectively; p is pressure; ρ is density calculated from the temperature T and salinity S; f is the Coriolis parameter; g is the gravitational acceleration; ρ_o is a reference density; h is water depth; K_m and K_h are the vertical eddy viscosity and diffusivity coefficients; and A_m and A_h are the horizontal eddy viscosity and diffusivity coefficients. The vector operators ∇, ∇_h and $\vec{u}$ are defined by

$$\nabla=\left(\frac{\partial}{\partial x},\frac{\partial}{\partial y},\frac{\partial}{\partial z}\right),\ \nabla_h=\left(\frac{\partial}{\partial x},\frac{\partial}{\partial y}\right),\quad \vec{u}=(u,v,w). \tag{A9}$$

[39] **Acknowledgments.** The authors wish to thank Liang Wang, Jun Zhao, Mike Dowd, Keith Thompson, John Cullen, Marlon Lewis and two anonymous reviewers for their useful suggestions and comments, Alex Hay and Douglas Schillinger for providing the buoy, ADCP and PT sensor measurements in Lunenburg Bay, Richard Davis for providing the optical and hydrographic measurements in the bay, Brian Petrie for providing the hydrographic measurements at station 2 along Halifax line, and Blair Greenan for providing the minilog temperature measurements in the bay. This study is part of the CMEP project funded by the Canadian Foundation for Climate and Atmospheric Sciences (CFCAS). Authors R.J.G and J.S. are also supported by NSERC, MARTEC (a Halifax-based company), and MSC through the NSERC/MARTEC/MSC Industrial Research Chair in "Regional Ocean Modeling and Prediction".

References

Davies, A. M., and R. A. Flather (1978), Computing extreme meteorologically induced currents with application to the northwest European continental shelf, *Cont. Shelf Res.*, *7*, 643–683.

Dietrich, D. E. (1997), Application of a modified Arakawa 'a' grid ocean model having reduced numerical dispersion to the Gulf of Mexico circulation, *Dyn. Atmos. Oceans*, *27*, 201–217.

Durski, S. M., S. M. Glenn, and D. B. Haidvogel (2004), Vertical mixing schemes in the coastal ocean, Comparison of the level 2.5 Mellor-Yamada scheme with an enhanced version of the K profile parameterization, *J. Geophys. Res.*, *109*, C01015, doi:10.1029/2002JC001702.

Emery, W. J., and R. E. Thomson (1998), *Data Analysis Methods in Physical Oceanography*, Elsevier, 638 pp.

Large, W. G., J. C. McWilliams, and S. C. Doney (1994), Oceanic vertical mixing: A review and a model with a nonlocal boundary layer parameterization, *Rev. Geophys.*, *32*, 363–403.

Lu, Y., D. G. Wright, and D. Brickman (2001), Internal tide generation over topography: Experiments with a free-surface z-level ocean model, *J. Atmos. Oceanic. Technol.*, *18*, 1076–1091.

Orlanski, I. (1976), A simple boundary condition for unbounded hyperbolic flows, *J. Comput. Phys.*, *21*, 251–269.

Paulson, C. A., and J. J. Simpson (1977), Irradiance measurements in the upper ocean, *J. Phys. Oceanogr.*, *7*, 952–956.

Pawlowicz, R., B. Beardsley, and S. Lentz (2002), Classical tidal harmonic analysis including error estimates in MATLAB using T_TIDE, *Comput. Geosci.*, *28*, 929–937.

Sheng, J., and L. Wang (2004), Numerical study of tidal circulation and nonlinear dynamics in Lunenburg Bay, Nova Scotia, *J. Geophys. Res.*, *109*, C10018, doi:10.1029/2004JC002404.

Sheng, J., J. Zhao, and L. Zhai (2008), Examination of circulation, dispersion, and connectivity in Lunenburg Bay of Nova Scotia using a nested-grid circulation model, *J. Mar. Syst.*, (in press).

Smagorinsky, J. (1963), General circulation experiments with the primitive equation. I. The basic experiment, *Mon. Weather Rev.*, *21*, 99–165.

Sturley, D. R. M., and A. J. Bowen (1996), A model for contaminant transport in Lunenburg Bay, Nova Scotia, *Sci. Total Environ.*, *179*, 161–172.

Thompson, K. R., and J. Sheng (1997), Subtidal circulation on the Scotian Shelf: Assessing the hindcast skill of a linear, barotropic model, *J. Geophys. Res.*, *102*, 24,987–25,003.

Thompson, K. R., D. E. Kelley, D. Sturley, B. Topliss, and R. Leal (1998), Nearshore circulation and synthetic aperture radar: An exploratory study, *Int. J. Remote Sens.*, *19*, 1161–1178.

Thuburn, J. (1996), Multidimensional flux-limited advection schemes, *J. Comput. Phys.*, *123*, 74–83.

Wang, L., J. Sheng, A. E. Hay, and D. J. Schillinger (2007), Storm-induced circulation in Lunenburg Bay of Nova Scotia, *J. Phys. Oceanogr.*, *37*, 873–895.

Zhai, L., J. Sheng, and R. J. Greatbatch (2007), Observations of the dynamical response of a coastal embayment to wind, tide, and buoyancy forcing, *Cont. Shelf Res.*, doi:10.1016/j.csr.2007.07.001.

Zhai, L., J. Sheng, and R. J. Greatbatch (2008), Baroclinic dynamics of wind-driven circulation in a stratified bay: A process study, *Cont. Shelf Res.*, submitted.

R. J. Greatbatch, J. Sheng, and L. Zhai, Department of Oceanography, Dalhousie University, Halifax, NS, Canada, B3H 4J1. (li.zhai@phys.ocean.dal.ca)